Title

Engineering correlated insulators in bilayer graphene with a remote Coulomb superlattice

Journal

Nature Materials, 23(2)

ISSN

1476-1122

Authors

Zhang, Zuocheng

Xie, Jingxu

Zhao, Wenyu

et al.

Publication Date

2024-02-01

DOI

10.1038/s41563-023-01754-3

Peer reviewed

Title

Engineering correlated insulators in bilayer graphene with a remote Coulomb superlattice

Author list

Zuocheng Zhang[1*], Jingxu Xie[1,2,3*], Wenyu Zhao[1], Ruishi Qi[1,3], Collin Sanborn[1], Shaoxin Wang[1], Salman Kahn[1], Kenji Watanabe[4], Takashi Taniguchi[5], Alex Zettl[1,3,6], Michael Crommie[1,3,6], Feng Wang[1,3,6]†

Affiliations

[1] Department of Physics, University of California at Berkeley, Berkeley, California 94720, United States

[2] Graduate Group in Applied Science and Technology, University of California at Berkeley, Berkeley, California 94720, United States

[3] Material Science Division, Lawrence Berkeley National Laboratory, Berkeley, California 94720, United States

[4] Research Center for Functional Materials, National Institute for Materials Science, 1-1 Namiki, Tsukuba 305-0044, Japan

[5] International Center for Materials Nanoarchitectonics, National Institute for Materials Science, 1-1 Namiki, Tsukuba 305-0044, Japan

[6] Kavli Energy NanoSciences Institute at University of California Berkeley and Lawrence Berkeley National Laboratory, Berkeley, California 94720, United States

* These authors contributed equally to this work

† Correspondence to: fengwang76@berkeley.edu

Abstract:

Electron superlattices allow the engineer of correlated and topological quantum phenomena. The recent emergence of moiré superlattices in two-dimensional (2D) heterostructures has led to exciting quantum phenomena discoveries. However, the requirement of the moiré pattern poses stringent limitations, and its potential cannot be switched on and off. Here, we demonstrate remote engineering and on/off switching of correlated states in bilayer graphene. Employing a remote Coulomb superlattice realized by localized electrons in a twisted bilayer WS_2, we impose a Coulomb superlattice in the bilayer graphene with period and strength determined by the twisted bilayer WS_2. When the remote superlattice is turned off, the two-dimensional electron gas (2DEG) in the bilayer graphene is described by a Fermi liquid, when it is turned on, correlated insulating states at both integer and fractional filling factors emerge. This approach enables in-situ control of correlated quantum phenomena in 2D materials hosting a 2DEG.

Main text:

A periodic potential, also known as a superlattice, can strongly modify the behavior of electrons in materials[1]. Two types of superlattice structures, the moiré superlattice and lithographic-patterned superlattice, have been utilized to engineer quantum phenomena in 2D materials. The moiré superlattice emerges naturally in the twisted stack of van der Waals heterostructures. It features almost perfect periodic potential at the nanometer scale and has enabled the discovery of many fascinating quantum phenomena, ranging from correlated insulators[2–5], superconductivity[4,5], Chern insulators[5,6] to moiré excitons[6–8], generalized Wigner crystal states[6–10] and correlated interlayer exciton insulator[11–14]. However, the creation of a moiré pattern requires specific material combinations, and the moiré potential cannot be turned on and off for a given moiré heterostructure. In comparison, the lithographic-patterned superlattice has tunability in both the superlattice symmetry and magnitude, enabling the observation of fractal Hofstadter spectra[15], anisotropic flat band[16], and replica Dirac cones[17] in graphene. However, achieving a perfect nanometer-scale lithographic-patterned electronic superlattice is challenging in the lithographic process. It will be desirable to achieve a superlattice design that combines the advantage of moiré superlattice and lithographic-patterned superlattice, which would greatly aid in the exploration of tunable correlated quantum phenomena.

In this work, we demonstrate such precise and tunable superlattice potential using a remote Coulomb superlattice configuration (Fig. 1a). The superlattice potential is generated by strongly localized electrons at the moiré lattice site in a close-to-60-degree twisted bilayer WS_2 in close proximity of the bilayer graphene layer. The period of the Coulomb superlattice is determined by the moiré period of the twisted bilayer WS_2, which can be controlled by the twist angle between the two WS_2 layers (Supplementary Fig. S1). The magnitude of the superlattice potential is

controlled by the number of localized electrons at the twisted bilayer WS_2 moiré lattice site. Twisted bilayer WS_2 is a compelling choice for this type of device because close to 60 degrees it is predicted to have particularly strong moiré potential and extremely flat moiré minibands[18]. To demonstrate this tunable remote Coulomb superlattice, we choose the bilayer graphene as the active material that hosts the 2D electron gases. Bernal stacked bilayer graphene and its moiré superlattice with hexagonal boron nitride (hBN) have been extensively studied previously[19–24]. These material systems exhibit many interesting properties, including a field tunable semiconductor bandgap[20], Hofstadter butterfly physics[25–27], and correlated phases under high vertical electric field[22–24]. However, pristine bilayer graphene has not shown correlated insulator states due to periodic potential modulation. In our remote Coulomb superlattice device, the bilayer graphene is separated from the twisted bilayer WS_2 by a thin hBN layer. We typically choose an hBN thickness of 3 nm to 5 nm so that the remote Coulomb potential could be maximized while the leakage current between bilayer graphene and the remote Coulomb superlattice is sufficiently low. At the same time, we expect that the hBN will strongly suppress the induced spin-orbital coupling between the WS_2 and graphene layer because the electron wavefunction overlap between WS_2 and graphene layer is decreased by many orders of magnitude.

Because of the strong interlayer Coulomb interaction, the bilayer graphene can experience a strong superlattice potential from the localized electrons of the twisted bilayer WS_2. The remote Coulomb superlattice can be turned on and off in situ by simply controlling the electron density in the twisted bilayer WS_2. We show that the electrons in bilayer graphene are largely described by a Fermi liquid when the remote Coulomb superlattice is turned off, but can develop strongly correlated insulating states at both integer and fractional filling factors when the remote Coulomb superlattice is turned on. Previously, interlayer exciton insulator is realized when the WS_2/WSe_2

moiré superlattice is in proximity to another WSe_2 monolayer[12,13]. Here, we employ twisted WS_2 with a deep moiré potential, enabling us to localize multiple electrons in a single moiré unicell. These localized electrons create a strong remote Coulomb superlattice, offering a powerful and flexible way to control correlated insulator states in any 2D materials. A perfect remote Coulomb superlattice depends on an ideal underlying moiré superlattice. However, inhomogeneity of the moiré superlattice[36,37] due to local twist angle and strain variation is almost unavoidable in real van der Waals heterostructure devices. This moiré inhomogeneity could affect the correlated insulator states resulting from the remote Coulomb superlattice, just as it affects the correlated states in regular moiré superlattice.

Figure 1a shows a schematic of a double-layer heterostructure with three gates, the top gate (V_t), bottom gate (V_b), and bias gate (V_{bias}), which allow us to control the carrier doping in both the twisted bilayer WS_2 (outlined by the red and yellow lines in the optical microscopy image in Fig. 1b) and the bilayer graphene (outlined by the black lines in Fig. 1b). Figure 1c illustrates the band alignment of the bilayer graphene and twisted bilayer WS_2. The conduction band minimum and valence band maximum of bilayer graphene are within the bandgap of twisted bilayer WS_2 (ref. [28]), and their energy offset (around ~0.4 eV between the conduction band minimums) can be modified by the vertical electrical field generated by the gate voltages. The bias voltage V_{bias} controls the relative chemical potential between the twisted bilayer WS_2 and bilayer graphene layers. The equilibrium state is governed by the relation[29]:

$$\mu_{WS2}(n_{WS2}) - \mu_{bigr}(n_{bigr}) = -eV_{bias} + eE_m d_m$$

where μ_{WS2} and μ_{bigr} are the chemical potential in twisted bilayer WS_2 and bilayer graphene, respectively. n_{WS2} is the electron density in twisted bilayer WS_2 and n_{bigr} is the electron density in the bilayer graphene, d_m is the thickness of the middle hBN layer, E_m is the electric field across the middle hBN layer, and e is the electron charge.

Figure 2 shows a 2D color plot of four-terminal resistance as a function of V_t and V_{bias} with the bottom gate voltage fixed at V_b = -16 V. The measurement temperature is at T = 18 K. The carrier doping in the twisted bilayer WS_2 and the bilayer graphene divide the plot into four regions. On the left side (at V_t < 1 V), the system is overall hole-doped, and the holes are in the bilayer graphene layer. The twisted WS_2 remains charge neutral. On the right side (at V_t >1 V), the system is overall electron-doped, but the charge distribution between the twisted bilayer WS_2 and bilayer graphene depends on the magnitude of V_t and V_{bias}. At V_{bias} > -0.7 V, electrons are first doped into the bilayer graphene layer, with the twisted bilayer WS_2 being charge neutral when V_t is increased (top middle region and on the left of the yellow dashed line). With increased V_t, both the twisted bilayer WS_2 and the bilayer graphene can become electron-doped (top right region and on the right of the yellow dashed line). The yellow dashed line, separating these two regions, is estimated by optical spectroscopy measurement of electron doping in the twisted WS_2 layer (Supplementary Fig. S2). At large negative V_{bias} and large V_t, it is possible to achieve electron doping in the twisted bilayer WS_2 but hole doping in the bilayer graphene layer (bottom right region). The charge neutral point of bilayer graphene is characterized by a large electrical resistance, which clearly delineates the transition between electron and hole doping in the bilayer graphene layer.

The bilayer graphene charge neutral line in the phase diagram allows us to probe the chemical potential of insulating states in the electron-doped twisted bilayer WS_2 (Ref. [30–33]). For a fixed V_b and $\mu_{bigr}(n_{bigr} = 0) = 0$, μ_{WS2} scales linearly with V_{bias}, while n_{WS2} scales linearly with V_t

(Methods). Therefore, the dispersion behavior of the bilayer graphene charge neutral line reflects the evolution of μ_{WS2} (right axis in Fig. 2) as a function of the electron doping n_{WS2} of the twisted bilayer WS_2 (top axis in Fig. 2).

The chemical potential μ_{WS2} decreases significantly with the increasing carrier concentration at low densities and approaches a constant value at high densities. This can be understood from the exchange and correlation effects of the 2D electrons: the exchange interaction and electron correlation reduce the close proximity of different electrons, therefore reduce the total energy and the chemical potential compared to a homogeneous electron distribution[29,34]. In addition to this general trend, μ_{WS2} shows several discrete jumps at specific electron densities, corresponding to the presence of insulating gaps[30–33]. The electron densities associated with the strongest insulating gaps (denoted by yellow arrows in Fig. 2) are at integer multiples 1 and 2 of $0.23\times10^{12}/cm^2$ (Extended Data Fig. 1 and 2). These can be attributed to insulating states formed at the integer filling of the moiré superlattice in twisted bilayer WS_2, where the filling factors are $\nu_{WS2} = 1$ and 2 and the moiré density is $n_{0WS2} = 0.23 \times 10^{12}/cm^2$. The corresponding twist angle of the twisted WS_2 is 59.2 degrees, and the moiré period is 22 nm in this device. In addition to the prominent insulating states discussed above, there are several distinct chemical potential jumps at other filling factors, including at relatively high electron densities with corresponding larger filling factors. The clear observation of insulating behavior at a large filling factor is rather unusual in moiré heterostructures[35]. It is consistent with the theoretical prediction of extremely strong correlation and flat moiré minibands in close-to-60-degree twisted WS_2 layer[18].

When electrons are localized at the moiré lattice site in the twisted bilayer WS_2, they establish a remote Coulomb superlattice in the nearby bilayer graphene layer with a periodicity of 22 nm. The bilayer graphene will experience the periodic Coulomb superlattice potential due to the strong

interlayer Coulomb interaction. Correlated insulator states are expected when the generated flat band is filled in bilayer graphene. To better visualize the correlated insulator states from the remote Coulomb superlattice, we plot the bilayer graphene resistance R_{xx} as a function of V_b and V_t at a fixed bias gate voltage V_{bias} = -0.8 V in Fig. 3a. The devices are kept at a nominal temperature of T = 10 mK unless otherwise specified.

In the parameter space of V_t-V_b, we again see four different regions depending on the doping of the twisted WS_2 (intrinsic or electron-doped) and the bilayer graphene (electron- or hole-doped). Let's focus on the top right corner of this plot, where the twisted bilayer WS_2 is strongly electron-doped (with an almost constant μ_{WS2}) and a remote Coulomb superlattice is present. In this region, V_t and V_b mostly control the carrier doping in the twisted bilayer WS_2 and the bilayer graphene, respectively. Figure 3b displays a zoomed-in plot of the area indicated by the white dashed rectangle in Fig. 3a. The white dashed line delineates points with the highest resistance, corresponding to the charge neutral line (CNL) in bilayer graphene. The bilayer graphene is hole-doped (electron-doped) in the region left (right) to this CNL. The resistance in the bilayer graphene remains rather high over an extended doping area due to correlation effects from the remote Coulomb superlattice. This correlation effect is asymmetric to the electron and hole doping: holes doped into the bilayer graphene layer experience an attractive potential from the Coulomb superlattice and exhibit stronger correlation effects. Consequently, we observe a well-defined correlated insulator state at hole doping of $0.23 \times 10^{12}/\text{cm}^2$ in the bilayer graphene, corresponding to the hole filling factor of ν_{bigr} = 1 in the remote Coulomb superlattice. The insulating states at ν_{bigr} = 2 and 4 are shown in the Supplementary Fig. S3. In addition, several correlated insulator states are also present below the ν_{bigr} = 1 filling factor. These correlated insulator states at non-integer filling factors are weaker and show somewhat complex behavior. We indicate three of these

non-integer insulating states in Fig. 3b and tentatively assign them to generalized Wigner crystal states at ν_{bigr} = 1/3, 1/2, and 2/3. The weaker resistance peaks away from the 1/3, 1/2, and 2/3 are likely due to fluctuations from moiré superlattice inhomogeneity, which is most significant for small twist angle samples. The moiré superlattice inhomogeneity is weaker in Device III, which has a larger twist angle of 58.6 degrees. As a result, the magnetic field induced correlated insulator states at 1/3 and 2/3 fillings in Device III (Extended Data Fig. 3) are cleaner and more prominent.

Figure 3c shows the temperature dependence of the resistance in the correlated insulator states, where the bilayer graphene electron density is controlled by V_b with fixed V_t = 3.5 V and V_{bias} = -0.8 V. The R_{xx} values at ν_{bigr} = 1, 2/3, 1/2, 1/3, and 0 gradually decrease as the temperature is increased from 10 mK to 25 K, consistent with the insulating behavior. The carrier density shows a slight shift with the temperatures for fixed gate voltages, which may be related to high contact resistances of twisted bilayer WS_2 at low temperatures (Extended Data Fig. 4). The thermally activated resistance behavior at the ν_{bigr} = 1 correlated insulator state is analyzed in Extended Data Fig. 5, from which we can estimate a thermal activation gap of 59 K. The correlated insulators at fractional fillings disappear at higher temperatures and therefore have smaller activation gaps (Fig. 3c). We note that there is a lack of metallic behavior at electron densities between the correlated insulating states, presumably due to the inhomogeneity and disorder effects in Device I with a very small twist angle. Such inhomogeneity effect is much weaker in Device II, which has a larger twist angle of 58.7 degrees. As a result, we observe clear metallic behavior between the correlated insulating states in Device II, as shown in Extended Data Fig. 6.

The remote Coulomb superlattice can be switched on and off electrically, which allows in-situ control of the correlated states in bilayer graphene. The yellow dashed box of Fig. 3a shows a

region where the twisted WS_2 is intrinsic and the remote Coulomb superlattice is turned off. The line with the large resistance corresponds to the bilayer graphene charge neutral point (CNP). The CNP resistance of bilayer graphene depends strongly on the vertical electrical field: it increases significantly at a higher electrical field due to the opening of a semiconductor bandgap[20]. In the absence of the remote Coulomb potential, the bilayer graphene quickly becomes metallic with a low resistance upon hole doping, in striking contrast with the behavior with the remote Coulomb potential (Fig. 3b). (The behavior upon electron doping is more complex: insulating states are observed at finite electron doping levels. The origin of these insulating states is not currently understood and will require further investigation.).

Figure 4 further demonstrates the very different magnetotransport behavior of the bilayer graphene when the remote Coulomb superlattice is switched off (Fig. 4a) and on (Fig. 4b). The corresponding derivative data is shown in the Supplementary Fig. S4. The bilayer graphene 2DEG shows a Fermi liquid behavior in the absence of the remote Coulomb superlattice (V_t = 0 V and V_{bias} = 0 V). It develops well defined Landau fan diagram with quantized Hall resistance at the Landau level filling factor ν_{LL} = 4, 8, and 12 (Extended Data Fig. 7). The behavior is completely different when the remote Coulomb superlattice is turned on (V_t = 4 V and V_{bias} = -0.8 V). The Landau fan diagram disappears entirely (Fig. 4b). Instead, correlated insulator states at fixed carrier densities dominate the magnetotransport data. The ν_{bigr} = 1, 2, and 4 insulators become stronger with the magnetic field and persist over the whole magnetic field range. The correlated insulators at fractional filling factors exhibit a more complex magnetic field dependence, where several insulating states are present at a low magnetic field while a single strongly insulating state close to ν_{bigr} = 2/3 filling persists at the high magnetic field. Complete three-dimensional (3D) phase diagrams at two representative temperatures are shown in the Extended Data Fig. 4. The

maximum tunneling current between twisted WS_2 and bilayer graphene is around 1nA (Supplementary Fig. S5).

The remote Coulomb superlattice with different superlattice periods can be realized by changing the twist angle in the twisted bilayer WS_2. Figure 5 shows the experimental data for Device II with a WS_2 twist angle of 58.7 degrees, corresponding to a remote Coulomb superlattice period of 14 nm (Extended Data Fig. 8). Figure 5a displays the bilayer graphene resistance R_{xx} as a function of V_b and V_t at a fixed bias gate voltage V_{bias} = -0.55 V. The overall phase diagram can be divided into four regions based on the doping of the twisted WS_2 (intrinsic or electron-doped) and the bilayer graphene (electron or hole-doped), similar to those in Device I (Fig.3a). Let's first focus on the region where the twisted bilayer WS_2 is strongly electron-doped (e.g. within the black dash box) and the remote Coulomb superlattice is turned on. In addition to a resistance peak at the CNP in bilayer graphene, a correlated insulator state is clearly observed at $\nu_{bigr} = 1$, corresponding to one hole per superlattice site. An insulating state is also present at $\nu_{bigr} = 2$. The vertical electric field dependence of the insulating states at $\nu_{bigr} = 1$ and 2 are shown in Fig. 5b. These two insulating states are more pronounced at higher electric fields.

Figure 5c and 5d display the very different magnetotransport behavior of the bilayer graphene in Device II when the remote Coulomb superlattice is switched off and on, respectively. The typical Landau fan diagram, shown in Fig. 5c, demonstrates that the 2DEG in the bilayer graphene is largely described by the Fermi liquid when the remote Coulomb superlattice is turned off (V_t = 0 V and V_{bias} = 0 V). The Hall resistance is quantized at the Landau level filling factor ν_{LL} = 4, 8, and 12 (Extended Data Fig. 7). Figure 5d shows the magnetoresistance of the correlated insulator state when the remote Coulomb superlattice is turned on (V_t = 6 V and V_{bias} = - 0.4 V). The Landau fan again disappears completely. Instead, the correlated insulator state at $\nu_{bigr} = 1$ persists at all

magnetic fields, and its resistance increases with the strength of the magnetic field. Highly resistive states also emerge at $\nu_{bigr} < 1$ in high magnetic fields (Extended Date Fig. 9).

To demonstrate the moiré superlattice has reasonable homogeneity in our devices, we have further reproduced the data using the different electrical contacts[38] in Device II (Supplementary Fig. S6). All the data show very similar behavior, indicating a reasonably homogeneous moiré superlattice in Device II. Moreover, we have fabricated another device (Device III) with a different transfer method and gold top gate. Results very similar to Device II are also observed in Device III which has a comparable remote Coulomb superlattice period of 13 nm (Extended Data Fig. 4 and 10). The consistent behavior in multiple devices demonstrates that the moiré superlattices in our devices are reasonably homogeneous, and the correlated insulating state in bilayer graphene is can be achieved reliably using the remote Coulomb superlattice.

Acknowledgements

The dilution fridge measurements are supported by the U.S. Department of Energy, Office of Science, National Quantum Information Science Research Centers, Quantum Systems Accelerator. The device fabrication is supported by Army Research Office award W911NF2110176. The optical characterization is supported by the U.S. Department of Energy, Office of Science, Office of Basic Energy Sciences, Materials Sciences and Engineering Division (DE-AC02-05-CH11231), within the van der Waals Heterostructure Program (KCWF16). K.W. and T.T. acknowledge support from JSPS KAKENHI (Grant Numbers 19H05790, 20H00354, and 21H05233).

Author Contributions Statement

FW conceived the research. ZZ and JX fabricated the device and performed most of the experimental measurements together. WZ, RQ, SK, MC, and AZ contributed to the fabrication of van der Waals heterostructures. CS and SW help with transport measurements. ZZ, JX, and FW performed data analysis. KW and TT grew hBN crystals. All authors discussed the results and wrote the manuscript.

Competing Interests Statement

The authors declare that they have no competing interests.

Figure caption:

Figure 1 | Configuration of the remote Coulomb superlattice. a, A schematic of the heterostructure device composed of a twisted bilayer WS_2 and a bilayer graphene separated by a thin hBN layer. Three electrical voltages, the top gate (V_t), bottom gate (V_b), and bias voltage (V_{bias}), enable independent control of carrier density in the twisted bilayer WS_2 and the bilayer graphene. Electrons localized at the moiré lattice sites in the twisted bilayer WS_2 form a remote Coulomb superlattice that provides a periodic potential acting on 2D electrons in the bilayer graphene. **b,** Optical microscopy image of a representative double-layer heterostructure device. The bilayer graphene (bigr), outlined by the black line, is pre-patterned to have six electrodes. Current (I) is driven through two electrodes, and voltage (V_{xx}) is measured by the other two electrodes. The twisted bilayer WS_2 (tWS_2) is outlined by the red and yellow lines. The contacts to the twisted bilayer WS_2 are outlined by the grey lines. The top few-layer graphite (FLG) gate is

outlined by the white lines. **c,** Band alignment of the bilayer graphene and twisted bilayer WS_2. The chemical potential of the twisted bilayer WS_2 (μ_{WS2}) can be shifted by the bias voltage V_{bias} relative to the chemical potential of bilayer graphene (μ_{bigr}).

Figure 2 | Chemical potential measurement of the twisted bilayer WS_2. 2D color plot of four-terminal resistance (R_{xx}) as a function of V_t and V_{bias} with the bottom gate voltage fixed at V_b = -16 V. The data is collected at zero magnetic fields and at the temperature T = 18 K. On the left (right) of the yellow dashed line, the twisted bilayer WS_2 is intrinsic (electron-doped). In the right region, the charge neutral line of bilayer graphene, characterized by a large resistance, can be clearly identified. Along this bilayer graphene charge neutral line, the chemical potential (μ_{WS2}) and electron densities (n_{WS2}) of the twisted bilayer WS_2 can be directly calculated according to equations (1) and (2) in the Methods. The values of μ_{WS2} and n_{WS2} are indicated on the right and top axis, respectively. The chemical potential shows several discrete jumps at specific electron densities (denoted by the yellow and white arrows), corresponding to the insulating states formed at the different filling ν_{WS2} in the twisted bilayer WS_2 moiré superlattice. The two strongest chemical potential jumps, denoted by two yellow arrows, correspond to the insulating states formed at the integer filling factor ν_{WS2} = 1 and 2 in the twisted bilayer WS_2 moiré superlattice. The electron density separation between the two jumps is around $0.23 \times 10^{12}/cm^2$. It corresponds to a moiré superlattice period of 22 nm. Most of the other chemical potential jumps can be assigned to the integer filling of this moiré superlattice (Extended Data Fig. 2).

Figure 3 | Correlated insulator states in bilayer graphene when the remote Coulomb superlattice is turned on. a, 2D Color plot of R_{xx} as a function of bottom gate voltage V_b and top gate voltage V_t at V_{bias} = -0.8 V. The data is collected at zero magnetic fields and at the nominal temperature T = 10 mK. The phase diagram has four regions depending on the doping in bilayer graphene (electron- or hole-doped) and twisted bilayer WS_2 (intrinsic or electron-doped). When the remote Coulomb superlattice is turned off (yellow dashed box), the resistance in the bilayer graphene decreases quickly and becomes metallic upon hole doping. When the remote Coulomb superlattice is turned on (top right region), correlated insulator states appear in the bilayer graphene upon hole doping. Here V_t and V_b mostly control the carrier doping in the twisted WS_2 layer and the bilayer graphene layer, respectively. **b,** Zoomed-in color plot of the white dashed rectangle of **a**, where the remote Coulomb superlattice is turned on. The white dashed line corresponds to the charge neutral point of bilayer graphene. A well-defined correlated insulator state is observed in the bilayer graphene, corresponding to the hole filling factor of ν_{bigr} = 1 in the remote Coulomb superlattice. The other correlated insulator states below the ν_{bigr} = 1 are assigned to generalized Wigner crystal states at ν_{bigr} = 1/3, 1/2, and 2/3, respectively. **c,** The 2D color plot of R_{xx} as a function of temperature T and bottom gate voltage V_b. The bias gate is fixed at V_{bias} = -0.8 V, and the top gate is fixed at V_t = 3.5 V. The data is collected at zero magnetic fields. The R_{xx} value at ν_{bigr} = 1, 2/3, 1/2, and 1/3 gradually decreases with increasing temperature, confirming the insulating nature of correlated insulator states.

Figure 4 | In-situ switching between the Fermi liquid and correlated insulator states in bilayer graphene. a, The bilayer graphene exhibits clear quantum oscillations and Landau fans characteristic of a Fermi liquid when the remote Coulomb superlattice is turned off. (The twisted bilayer WS_2 is intrinsic at V_t = 0 V and V_{bias} = 0 V). The data is collected at the nominal temperature T = 10 mK. The magnetoresistance minimum corresponds to the gap between Landau levels. The filling factor (ν_{LL}) is determined by the quantized Hall resistance. Here the V_{cnp} is V_b = -7.80 V. **b,** Magnetic field dependence of correlated insulator states when the remote Coulomb superlattice is turned on (twisted bilayer WS_2 is highly electron-doped at V_t = 4 V and V_{bias} = -0.8 V). The data is collected at the nominal temperature T = 10 mK. The correlated insulator state at ν_{bigr} = 1 is nearly independent of the magnetic field, reflecting that the electrons in bilayer graphene are strongly correlated. Several insulating states at fractional filling factors are present at a low magnetic field, while a single strongly insulating state close to ν_{bigr} = 2/3 filling persists at the high magnetic field. Here the V_{cnp} is around V_b = 0.05 V.

Figure 5 | Remote Coulomb superlattice behavior in a second device with a superlattice period of 14 nm. a, The 2D color plot of R_{xx} as a function of top gate voltage V_t and bottom gate voltage V_b at V_{bias} = -0.55 V. The data is collected at zero magnetic fields and at the nominal temperature T = 10 mK. The phase diagram has four regions depending on the electron doping in the twisted bilayer WS_2 (intrinsic or electron-doped) and bilayer graphene (hole- or electron-

doped). When the remote Coulomb superlattice is turned on (black dashed box), the hole-doped bilayer graphene shows correlated insulator states at ν_{bigr} = 1 and 2. **b,** Vertical electric field dependence of the insulating state at ν_{bigr} = 1 and 2. The top gate voltage is at V_t = 6 V. The data is collected at zero magnetic fields and at the nominal temperature T = 10 mK. The correlated insulator states become more pronounced at the higher vertical electric field. **c,** Landau fan diagram when the remote Coulomb superlattice is turned off. (The twisted bilayer WS_2 is intrinsic at V_t = 0 V and V_{bias} = 0 V.) The data is collected at the temperature T = 10 mK. The filling factor ν_{LL} is determined by the quantized Hall resistance. Here the V_{cnp} is around V_b = -5 V. **d,** Magnetic field dependence of the correlated insulator states when the remote Coulomb superlattice is turned on. The bias gate voltage is at V_{bias} = -0.4 V, and the top gate voltage is at V_t = 6 V. The data is collected at the temperature T = 10 mK. A resistance peak at ν_{bigr} = 1 is always present at all magnetic fields, demonstrating the strong electron correlation when the remote Coulomb superlattice is turned on. Here the V_{cnp} is around V_b = -24 V.

References

1. Esaki, L. & Tsu, R. Superlattice and Negative Differential Conductivity in Semiconductors. *IBM J. Res. Dev.* **14**, 61–65 (1970).
2. Cao, Y. *et al.* Correlated insulator behaviour at half-filling in magic-angle graphene superlattices. *Nature* **556**, 80–84 (2018).
3. Chen, G. *et al.* Evidence of a gate-tunable Mott insulator in a trilayer graphene moiré superlattice. *Nat. Phys.* **15**, 237–241 (2019).
4. Balents, L., Dean, C. R., Efetov, D. K. & Young, A. F. Superconductivity and strong correlations in moiré flat bands. *Nat. Phys.* **16**, 725–733 (2020).
5. Andrei, E. Y. & MacDonald, A. H. Graphene bilayers with a twist. *Nat. Mater.* **19**, 1265–1275 (2020).
6. Mak, K. F. & Shan, J. Semiconductor moiré materials. *Nat. Nanotechnol.* **17**, 686–695 (2022).
7. Huang, D., Choi, J., Shih, C.-K. & Li, X. Excitons in semiconductor moiré superlattices. *Nat. Nanotechnol.* **17**, 227–238 (2022).
8. Regan, E. C. *et al.* Emerging exciton physics in transition metal dichalcogenide heterobilayers. *Nat. Rev. Mater.* **7**, 778–795 (2022).
9. Regan, E. C. *et al.* Mott and generalized Wigner crystal states in WSe_2/WS_2 moiré superlattices. *Nature* **579**, 359–363 (2020).
10. Xu, Y. *et al.* Correlated insulating states at fractional fillings of moiré superlattices. *Nature* **587**, 214–218 (2020).

11. Ma, L. *et al.* Strongly correlated excitonic insulator in atomic double layers. *Nature* **598**, 585–589 (2021).
12. Zhang, Z. *et al.* Correlated interlayer exciton insulator in heterostructures of monolayer WSe_2 and moiré WS_2/WSe_2. *Nat. Phys.* **18**, 1214–1220 (2022).
13. Gu, J. *et al.* Dipolar excitonic insulator in a moiré lattice. *Nat. Phys.* **18**, 395–400 (2022).
14. Chen, D. *et al.* Excitonic insulator in a heterojunction moiré superlattice. *Nat. Phys.* **18**, 1171–1176 (2022).
15. Forsythe, C. *et al.* Band structure engineering of 2D materials using patterned dielectric superlattices. *Nat. Nanotechnol.* **13**, 566–571 (2018).
16. Li, Y. *et al.* Anisotropic band flattening in graphene with one-dimensional superlattices. *Nat. Nanotechnol.* **16**, 525–530 (2021).
17. Dubey, S. *et al.* Tunable Superlattice in Graphene To Control the Number of Dirac Points. *Nano Lett.* **13**, 3990–3995 (2013).
18. Naik, M. H. & Jain, M. Ultraflatbands and Shear Solitons in Moiré Patterns of Twisted Bilayer Transition Metal Dichalcogenides. *Phys. Rev. Lett.* **121**, 266401 (2018).
19. Novoselov, K. S. *et al.* Unconventional quantum Hall effect and Berry's phase of 2π in bilayer graphene. *Nat. Phys.* **2**, 177–180 (2006).
20. Zhang, Y. *et al.* Direct observation of a widely tunable bandgap in bilayer graphene. *Nature* **459**, 820–823 (2009).
21. Zheng, Z. *et al.* Unconventional ferroelectricity in moiré heterostructures. *Nature* **588**, 71–76 (2020).
22. Zhou, H. *et al.* Isospin magnetism and spin-polarized superconductivity in Bernal bilayer graphene. *Science* **375**, 774–778 (2022).

23. de la Barrera, S. C. *et al.* Cascade of isospin phase transitions in Bernal-stacked bilayer graphene at zero magnetic field. *Nat. Phys.* **18**, 771–775 (2022).
24. Seiler, A. M. *et al.* Quantum cascade of correlated phases in trigonally warped bilayer graphene. *Nature* **608**, 298–302 (2022).
25. Dean, C. R. *et al.* Hofstadter's butterfly and the fractal quantum Hall effect in moiré superlattices. *Nature* **497**, 598–602 (2013).
26. Hunt, B. *et al.* Massive Dirac Fermions and Hofstadter Butterfly in a van der Waals Heterostructure. *Science* **340**, 1427–1430 (2013).
27. Ponomarenko, L. A. *et al.* Cloning of Dirac fermions in graphene superlattices. *Nature* **497**, 594–597 (2013).
28. Liu, Y., Stradins, P. & Wei, S.-H. Van der Waals metal-semiconductor junction: Weak Fermi level pinning enables effective tuning of Schottky barrier. *Sci. Adv.* **2**, e1600069.
29. Eisenstein, J. P., Pfeiffer, L. N. & West, K. W. Compressibility of the two-dimensional electron gas: Measurements of the zero-field exchange energy and fractional quantum Hall gap. *Phys. Rev. B* **50**, 1760–1778 (1994).
30. Kim, S. *et al.* Direct Measurement of the Fermi Energy in Graphene Using a Double-Layer Heterostructure. *Phys. Rev. Lett.* **108**, 116404 (2012).
31. Lee, K. *et al.* Chemical potential and quantum Hall ferromagnetism in bilayer graphene. *Science* **345**, 58–61 (2014).
32. Park, J. M., Cao, Y., Watanabe, K., Taniguchi, T. & Jarillo-Herrero, P. Flavour Hund's coupling, Chern gaps and charge diffusivity in moiré graphene. *Nature* **592**, 43–48 (2021).
33. Yang, F. *et al.* Experimental Determination of the Energy per Particle in Partially Filled Landau Levels. *Phys. Rev. Lett.* **126**, 156802 (2021).

34. Wigner, E. On the Interaction of Electrons in Metals. *Phys. Rev.* **46**, 1002–1011 (1934).
35. Slagle, K. & Fu, L. Charge transfer excitations, pair density waves, and superconductivity in moiré materials. *Phys. Rev. B* **102**, 235423 (2020).
36. Weston, A. *et al.* Atomic reconstruction in twisted bilayers of transition metal dichalcogenides. *Nat. Nanotechnol.* **15**, 592–597 (2020).
37. Shabani, S. *et al.* Deep moiré potentials in twisted transition metal dichalcogenide bilayers. *Nat. Phys.* **17**, 720–725 (2021).
38. Yankowitz, M. *et al.* Tuning superconductivity in twisted bilayer graphene. *Science* **363**, 1059–1064 (2019).

Methods

Heterostructure preparation:

We use polypropylene carbon (PPC) and polyethylene terephthalate glycol (PETG) based dry transfer technology[39] to subsequently pick up the two-dimensional flakes, which are first mechanically exfoliated from the bulk crystal on a SiO_2/Si substrate. The twisted WS_2 moiré bilayer is made by the tear and stack method[2] to have a close-to-60-degrees twist angle. The bilayer graphene is pre-patterned by atomic force microscopy (AFM) cutting to have six electrodes before the stacking process. The twisted WS_2 and bilayer graphene are separated by a hexagonal boron nitride (hBN) layer with an effective thickness of roughly 3 nm (Device I and II) and 5 nm (Device III). The double layers are further sandwiched by two hBN flakes. The top twisted bilayer WS_2 is contacted by the few-layer graphite (FLG), and the top gate is made of the FLG (Device I and II) or gold (Device III). The Device I and II is further capped by an hBN flake to help in device assembly. Finally, the whole stack is released onto a 90 nm (Device I) or 285 nm (Device II and III) SiO_2/Si substrate. The top dielectric hBN thickness is around 14 nm (Device I), 12 nm (Device

II), and 13 nm (Device III). The bilayer graphene is then directly contacted by the Cr/Au electrodes (5 nm Cr /50 nm Au), which is fabricated by standard e-beam lithography and e-beam evaporation.

Transport measurements:

The transport measurements are mainly performed in a dilution fridge (Bluefors) with a base temperature of T = 10 mK. All the signal wires are filtered at the mixing chamber flange (T = 10 mK) by the RC and RL filters (Qdevil) before reaching the sample. Keithley 6221 current source meter and Keithley 2182 nanometer are operated in the DC delta mode to measure the four-terminal resistance of bilayer graphene in Device I as Keithley 2182 nanovoltmeter has a typical input impedance of $R_{input} > 10$ GΩ. The amplitude of the alternating DC current is 1nA. The delay time in the delta mode is set at 300 ms. For Device II and III, the R_{xx} is measured by using the standard four-probe ac lock-in method with an AC current of 10 nA for a better signal-to-noise ratio. The frequency of AC current is around 17 Hz. DC delta mode is also used in the chemical potential measurement in Device II. Three gates, the top gate (V_t), bottom gate (V_b), and bias gate (V_{bias}) are applied by Keithley 2400, 2450 source meters, or 2502 picoammeter.

Optical measurements:

The optical measurements are performed in a cryostat with a temperature range down to T = 1.6 K (Quantum Design, Opticool). We use a supercontinuum laser as the light source for reflection contrast measurements. The light is focused on the sample by a 20X Mitutoyo objective with ~2 μm beam size. The reflected light is collected by the same objective and dispersed by a spectrometer before reaching the camera. The reflection contrast ($-\Delta R/R$) is calculated as $-(R_s - R_{ref})/(R_{ref} - R_{bkg})$, where R_s (R_{ref}) is the reflection spectrum with (without) the sample, R_{bkg} is the background spectrum.

Chemical potential measurements:

At the bilayer graphene charge neutral point ($n_{bigr} = 0$), the vertical electric field E_b across the bottom hBN/SiO_2 dielectric layer is equal to the vertical electric field E_m across the middle hBN dielectric layer with $E_b = E_m = \frac{0-V_b}{d_b} = -\frac{V_b}{d_b}$, where V_b is the bottom gate voltage, d_b is the thickness of the bottom dielectric hBN/SiO_2 dielectric layer (The dielectric constant of hBN and SiO_2 are both around 4). The vertical electric field E_t across the top hBN dielectric layer is given by $E_t = (V_t - E_m d_m)/d_t$, where d_t is the thickness of top dielectric layer. Here we choose $\mu_{bigr} = 0$ when the bilayer graphene is intrinsic ($n_{bigr} = 0$), the chemical potential of twisted bilayer WS_2 is given by:

$$\mu_{WS2}(n_{WS2}) = -eV_{bias} - e\frac{V_b}{d_b}d_m \qquad (1)$$

The electron density n_{WS2} of the twisted bilayer WS_2 is determined by the difference between E_t and E_m:

$$n_{WS2} = \frac{\varepsilon_0 \varepsilon_{hBN}}{e}(E_t - E_m)$$

As $E_t = (V_t - E_m d_m)/d_t$

$$n_{WS2} = \frac{\varepsilon_0 \varepsilon_{hBN}}{e}\left(\frac{V_t - E_m d_m}{d_t} - E_m\right)$$

$$n_{WS2} = \frac{\varepsilon_0 \varepsilon_{hBN}}{e}\frac{V_t}{d_t} + \frac{\varepsilon_0 \varepsilon_{hBN}}{e}(-E_m)\left(1 + \frac{d_m}{d_t}\right)$$

As $E_m = \frac{0-V_b}{d_b} = -\frac{V_b}{d_b}$,

$$n_{WS2} = \frac{\varepsilon_0 \varepsilon_{hBN}}{e}\frac{V_t}{d_t} + \frac{\varepsilon_0 \varepsilon_{hBN}}{e}\frac{V_b}{d_b}\left(1 + \frac{d_m}{d_t}\right)$$

Therefore,

$$n_{WS2} = \frac{\varepsilon_0 \varepsilon_{hBN}}{e}(E_t - E_m) = \frac{\varepsilon_0 \varepsilon_{hBN}}{e}\frac{V_t}{d_t} + \frac{\varepsilon_0 \varepsilon_{hBN}}{e}\frac{V_b}{d_b}\left(1 + \frac{d_m}{d_t}\right) \quad (2)$$

Here, $\varepsilon_0$is the vacuum permittivity, ε_{hBN} is the hBN dielectric constant.

For a fixed V_b and $\mu_{bigr}(n_{bigr} = 0)$, the second term in both equations (1) and (2) is a constant. As a result, μ_{WS2} scales linearly with V_{bias}, while n_{WS2} scales linearly with V_t.

Data availability

The data that support the findings of this study are available in https://doi.org/10.5061/dryad.w3r2280xx

Methods-only references

39. Wang, L. *et al.* One-Dimensional Electrical Contact to a Two-Dimensional Material. *Science* **342**, 614–617 (2013).

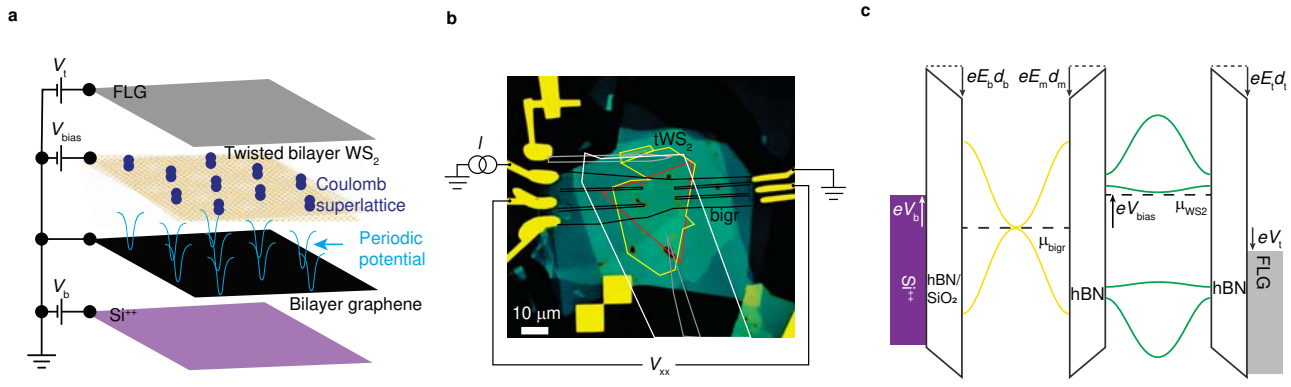
a
V_t
FLG
V_{bias}
Twisted bilayer WS_2
Coulomb superlattice
Periodic potential
V_b
Si^{++}
Bilayer graphene
b
I
tWS_2
bigr
10 μm
V_{xx}
c
$eE_b d_b$
$eE_m d_m$
$eE_t d_t$
eV_b
Si^{++}
hBN/ SiO_2
μ_{bigr}
hBN
eV_{bias}
μ_{WS2}
hBN
eV_t
FLG

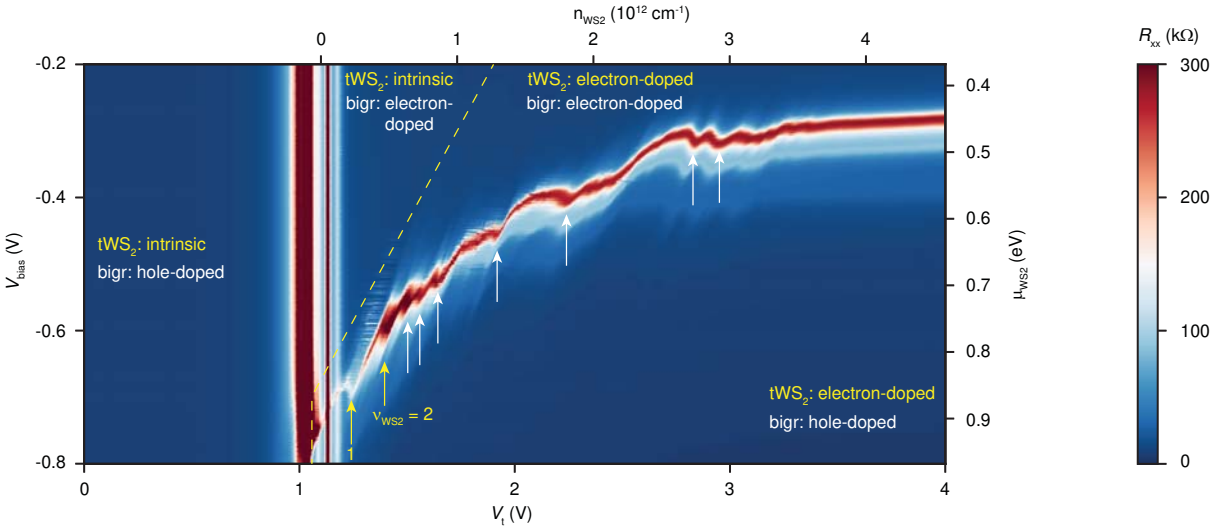
n_{WS2} (10^{12} cm^{-1})
0
1
2
3
4
-0.2
-0.4
-0.6
-0.8
V_{bias} (V)
V_t (V)
μ_{WS2} (eV)
0.4
0.5
0.6
0.7
0.8
0.9
R_{xx} (kΩ)
300
200
100
0
tWS$_2$: intrinsic
bigr: hole-doped
tWS$_2$: intrinsic
bigr: electron-doped
tWS$_2$: electron-doped
bigr: electron-doped
tWS$_2$: electron-doped
bigr: hole-doped
ν_{WS2} = 2
1

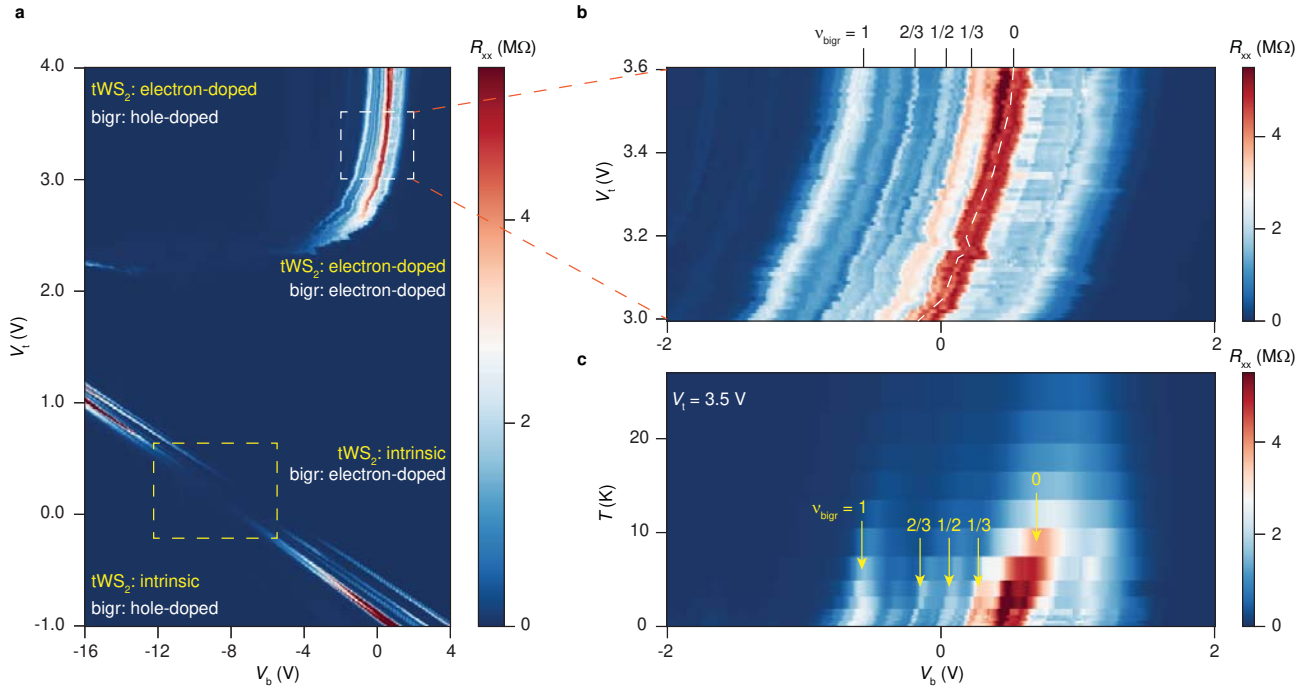
a
b
c
R_{xx} (MΩ)
tWS$_2$: electron-doped
bigr: hole-doped
tWS$_2$: electron-doped
bigr: electron-doped
tWS$_2$: intrinsic
bigr: electron-doped
tWS$_2$: intrinsic
bigr: hole-doped
V_t (V)
V_b (V)
ν_{bigr} = 1
2/3 1/2 1/3
0
V_t = 3.5 V
T (K)

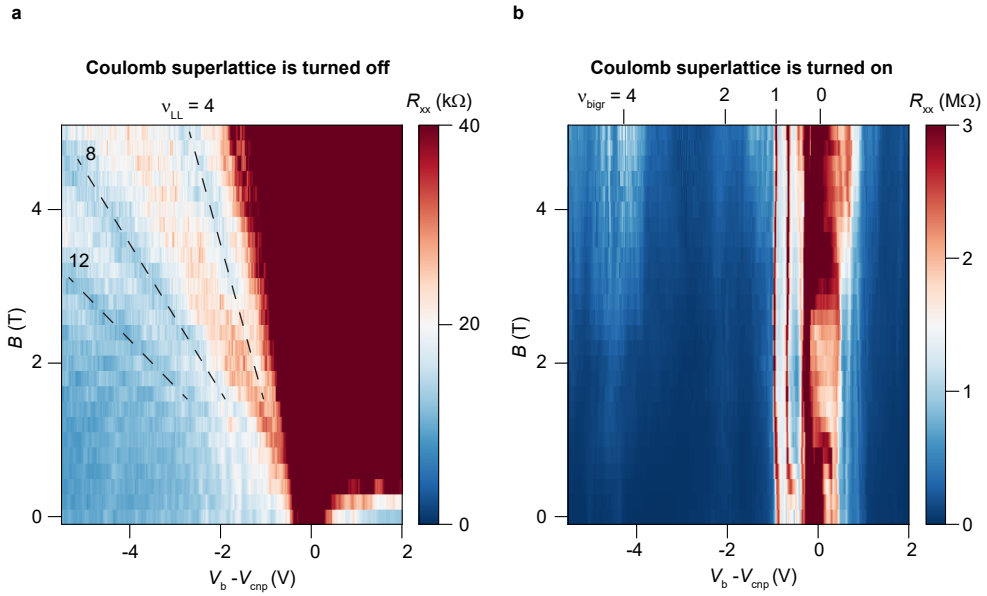
a
Coulomb superlattice is turned off
ν_{LL} = 4
R_{xx} (kΩ)
40
20
0
8
12
4
2
0
B (T)
-4
-2
0
2
V_b -V_{cnp} (V)
b
Coulomb superlattice is turned on
ν_{bigr} = 4
2
1
0
R_{xx} (MΩ)
3
2
1
0
4
2
0
B (T)
-4
-2
0
2
V_b -V_{cnp} (V)

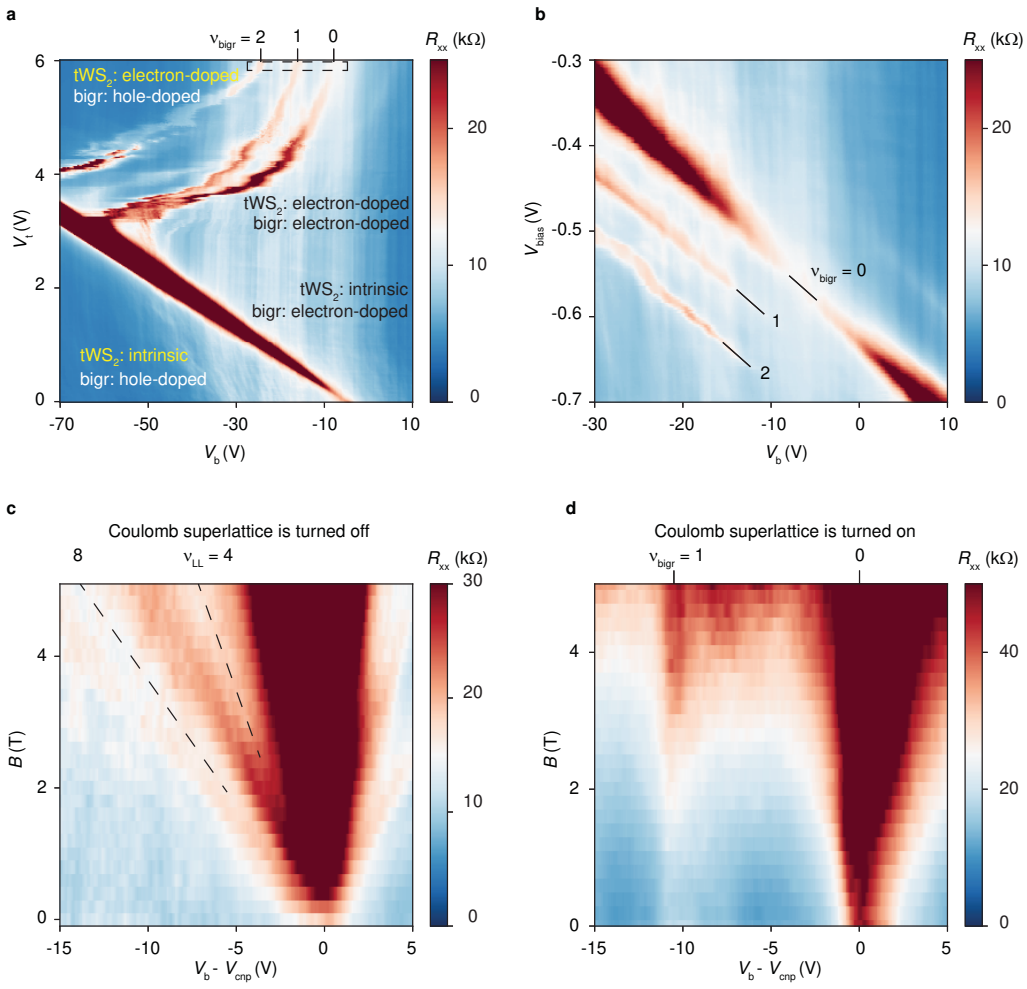
a
ν_{bigr} = 2
1
0
R_{xx} (kΩ)
tWS$_2$: electron-doped
bigr: hole-doped
tWS$_2$: electron-doped
bigr: electron-doped
tWS$_2$: intrinsic
bigr: electron-doped
tWS$_2$: intrinsic
bigr: hole-doped
V_t (V)
V_b (V)
b
R_{xx} (kΩ)
V_{bias} (V)
ν_{bigr} = 0
1
2
V_b (V)
c
Coulomb superlattice is turned off
8
ν_{LL} = 4
R_{xx} (kΩ)
B (T)
V_b - V_{cnp} (V)
d
Coulomb superlattice is turned on
ν_{bigr} = 1
0
R_{xx} (kΩ)
B (T)
V_b - V_{cnp} (V)

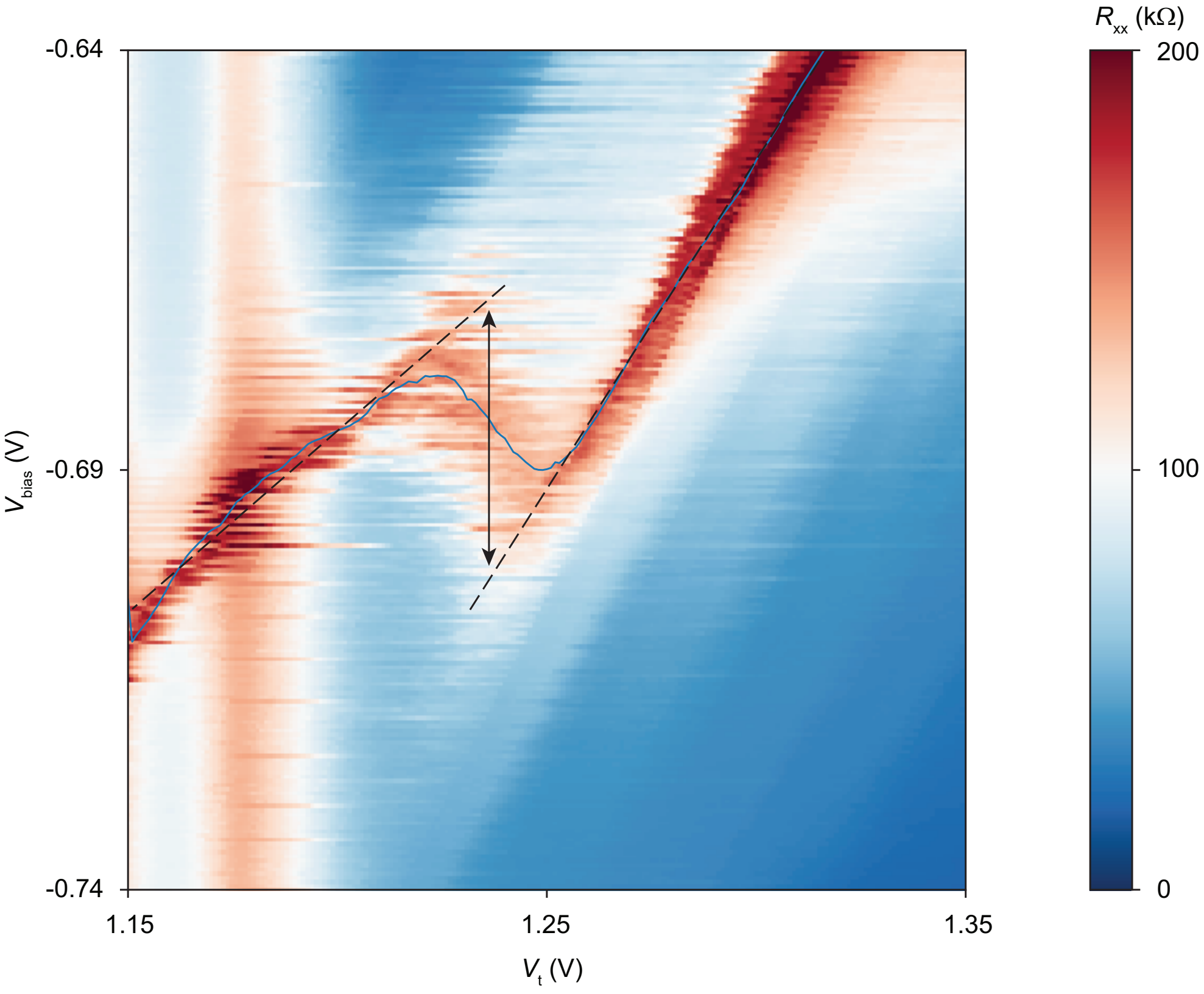
R_{xx} (kΩ)
200
100
0
-0.64
-0.69
-0.74
V_{bias} (V)
1.15
1.25
1.35
V_t (V)

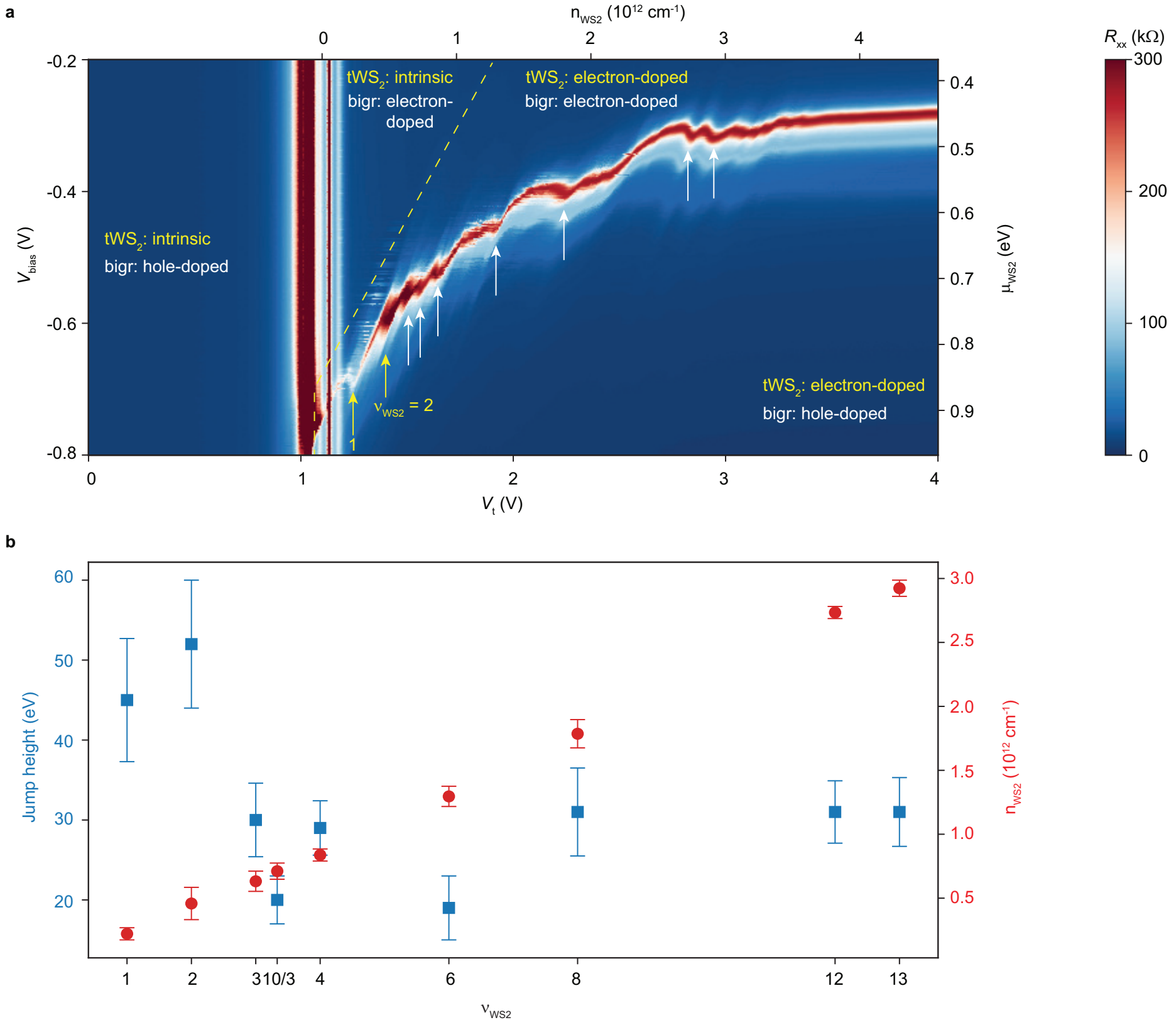
a
n_{WS2} (10^{12} cm^{-1})
R_{xx} (kΩ)
V_{bias} (V)
V_t (V)
μ_{WS2} (eV)
tWS$_2$: intrinsic
bigr: hole-doped
tWS$_2$: intrinsic
bigr: electron-doped
tWS$_2$: electron-doped
bigr: electron-doped
tWS$_2$: electron-doped
bigr: hole-doped
ν_{WS2} = 2
1
b
Jump height (eV)
n_{WS2} (10^{12} cm^{-1})
ν_{WS2}

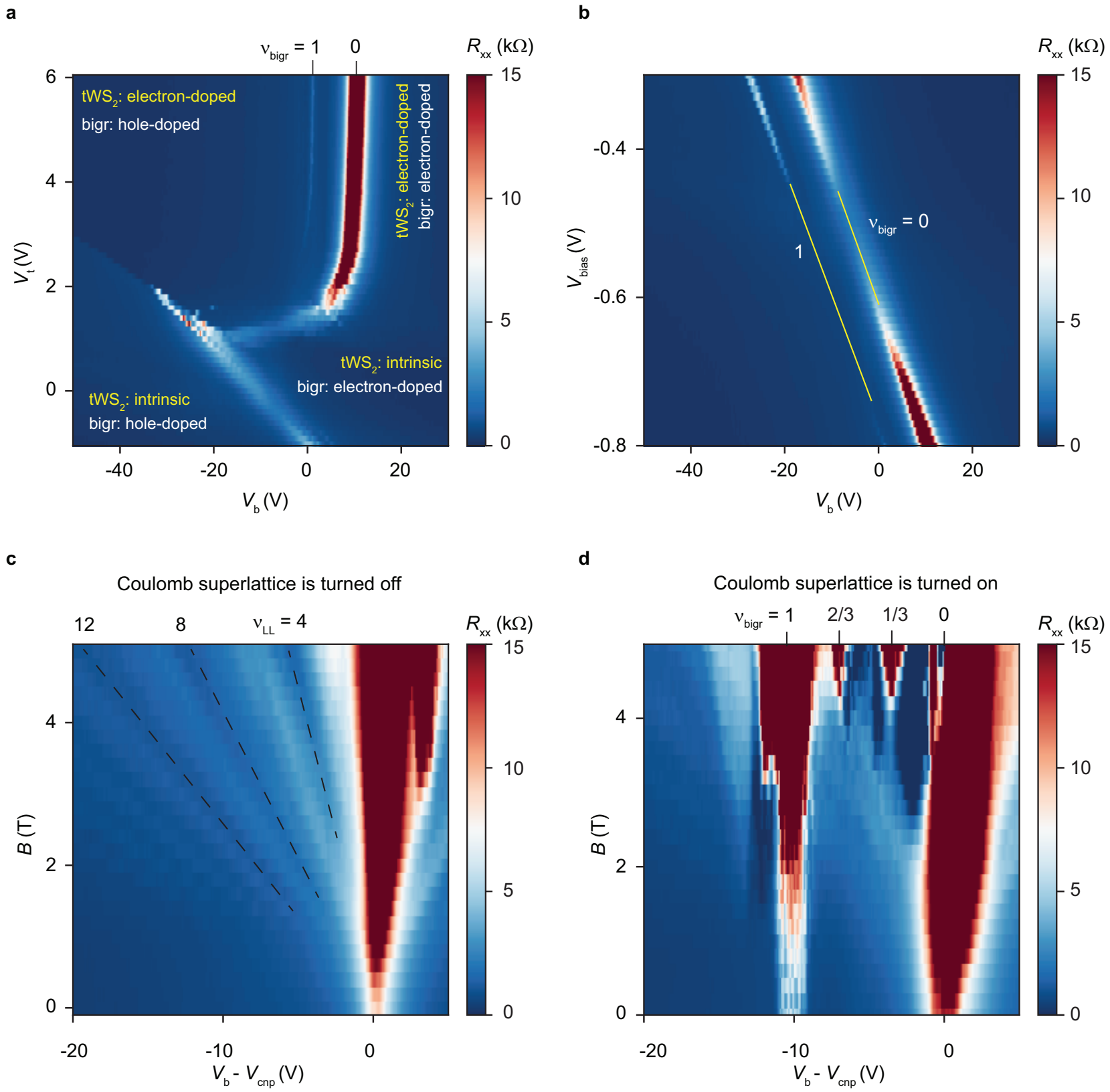
a
ν_{bigr} = 1
0
R_{xx} (kΩ)
15
10
5
0
6
4
2
0
V_t (V)
tWS$_2$: electron-doped
bigr: hole-doped
tWS$_2$: electron-doped
bigr: electron-doped
tWS$_2$: intrinsic
bigr: electron-doped
tWS$_2$: intrinsic
bigr: hole-doped
-40
-20
0
20
V_b (V)
b
R_{xx} (kΩ)
15
10
5
0
-0.4
-0.6
-0.8
V_{bias} (V)
ν_{bigr} = 0
1
-40
-20
0
20
V_b (V)
c
Coulomb superlattice is turned off
12
8
ν_{LL} = 4
R_{xx} (kΩ)
15
10
5
0
4
2
0
B (T)
-20
-10
0
V_b - V_{cnp} (V)
d
Coulomb superlattice is turned on
ν_{bigr} = 1
2/3
1/3
0
R_{xx} (kΩ)
15
10
5
0
4
2
0
B (T)
-20
-10
0
V_b - V_{cnp} (V)

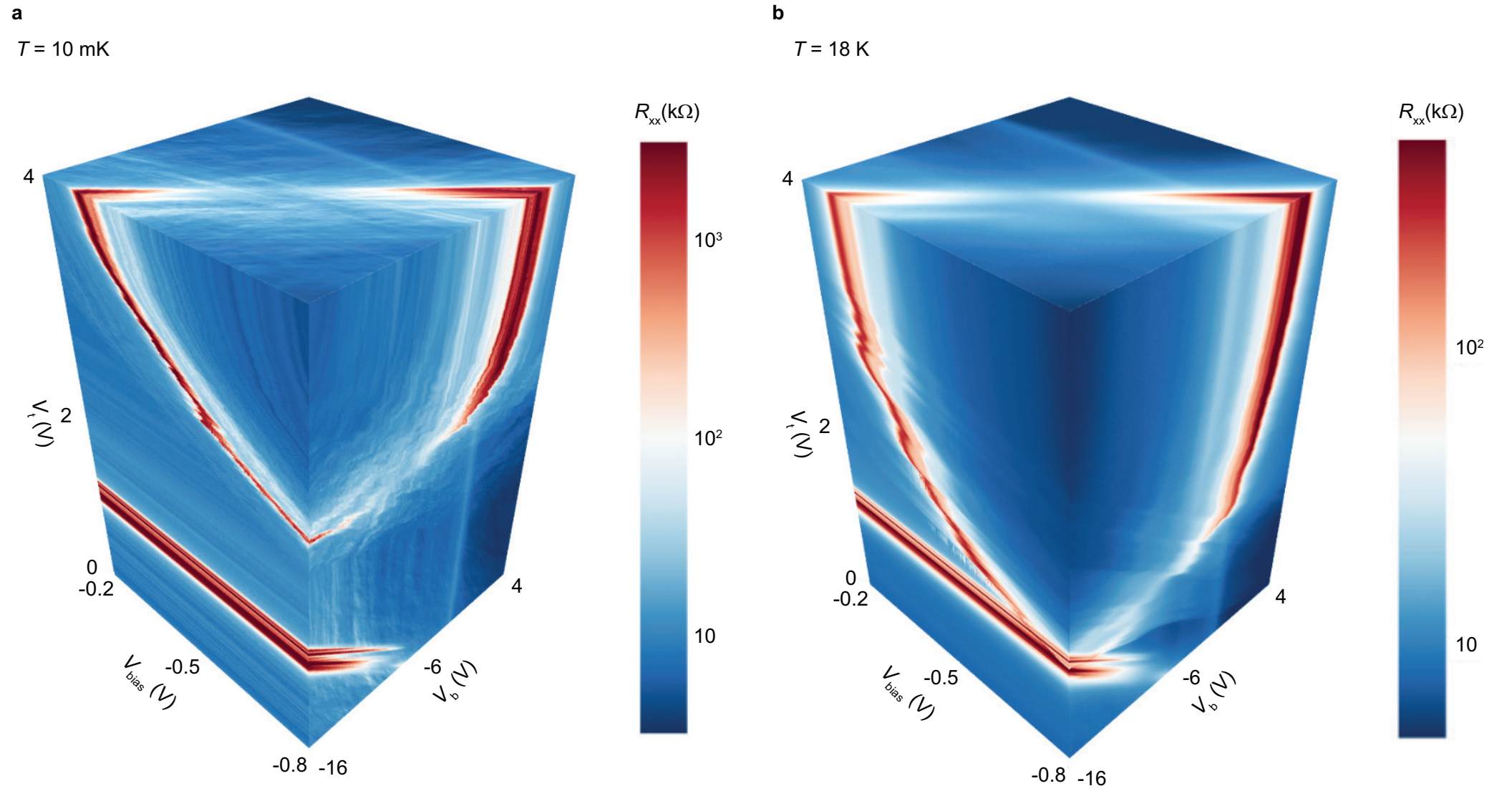
a
T = 10 mK
R_xx(kΩ)
10^3
10^2
10
4
2
0
-0.2
V_t (V)
V_bias (V)
-0.5
-0.8
-6
-16
V_b (V)
4
b
T = 18 K
R_xx(kΩ)
10^2
10
4
2
0
-0.2
V_t (V)
V_bias (V)
-0.5
-0.8
-6
-16
V_b (V)
4

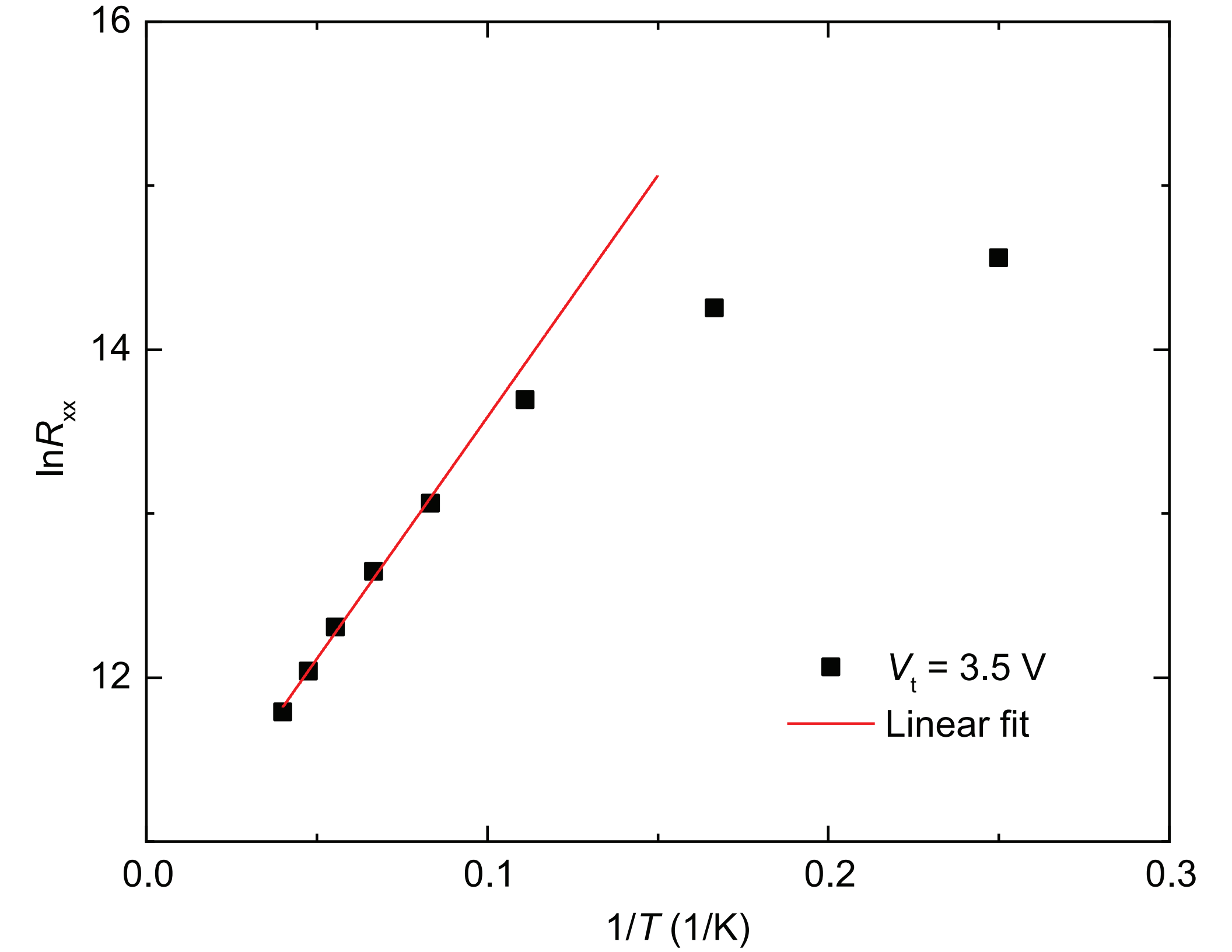
16
14
12
lnR_{xx}
0.0
0.1
0.2
0.3
1/T (1/K)
V_t = 3.5 V
Linear fit

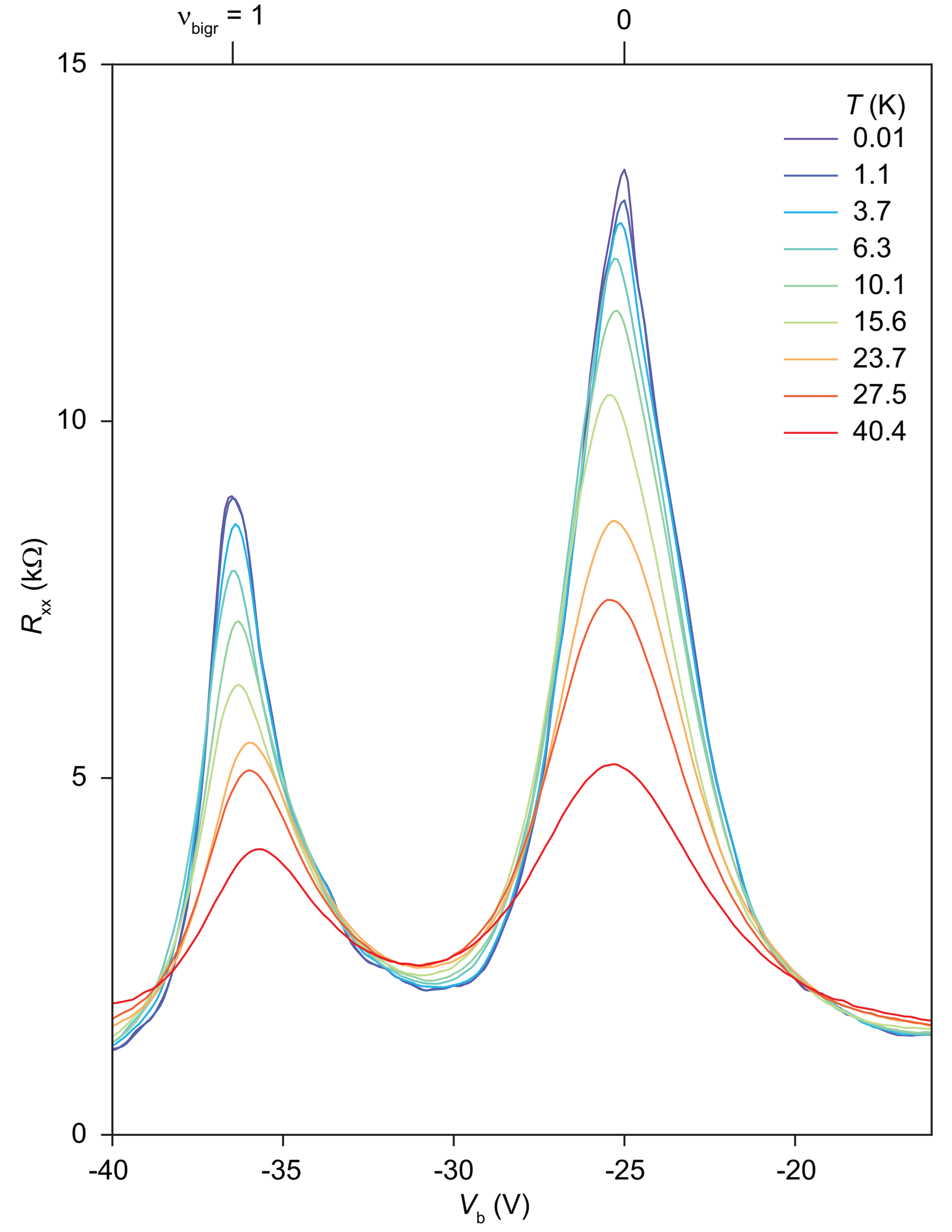
ν_{bigr} = 1
0
15
10
5
0
R_{xx} (kΩ)
-40
-35
-30
-25
-20
V_b (V)
T (K)
0.01
1.1
3.7
6.3
10.1
15.6
23.7
27.5
40.4

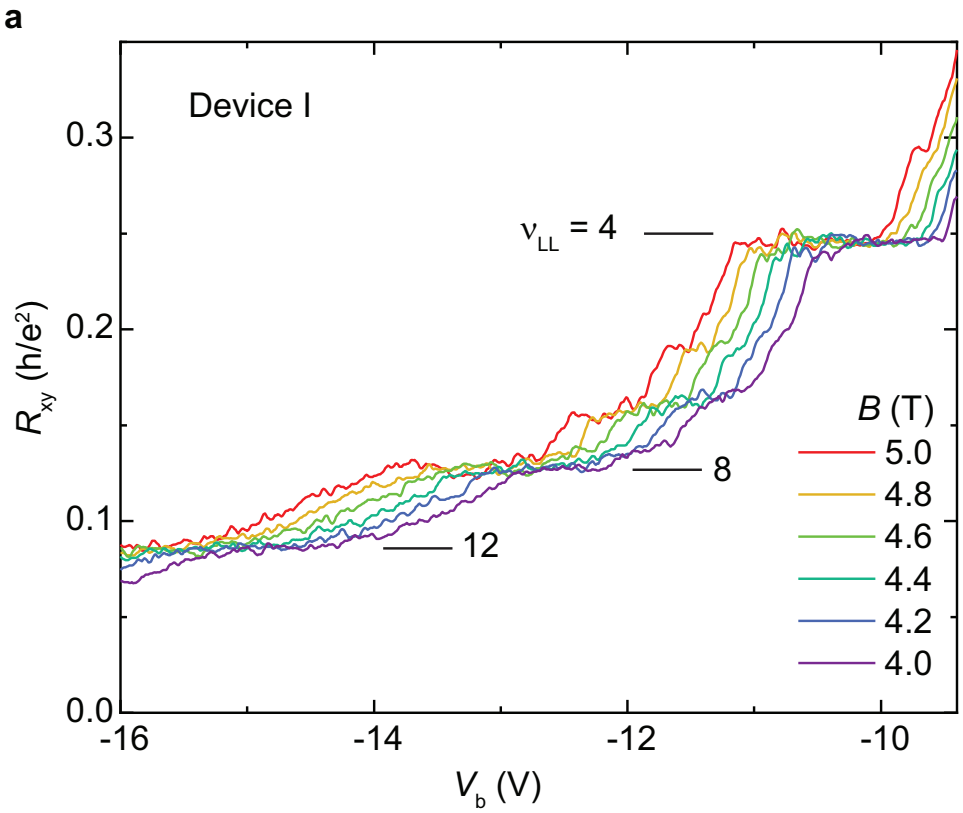
a
Device I
0.3
0.2
0.1
0.0
R_{xy} (h/e^2)
ν_{LL} = 4
8
12
B (T)
5.0
4.8
4.6
4.4
4.2
4.0
-16
-14
-12
-10
V_b (V)

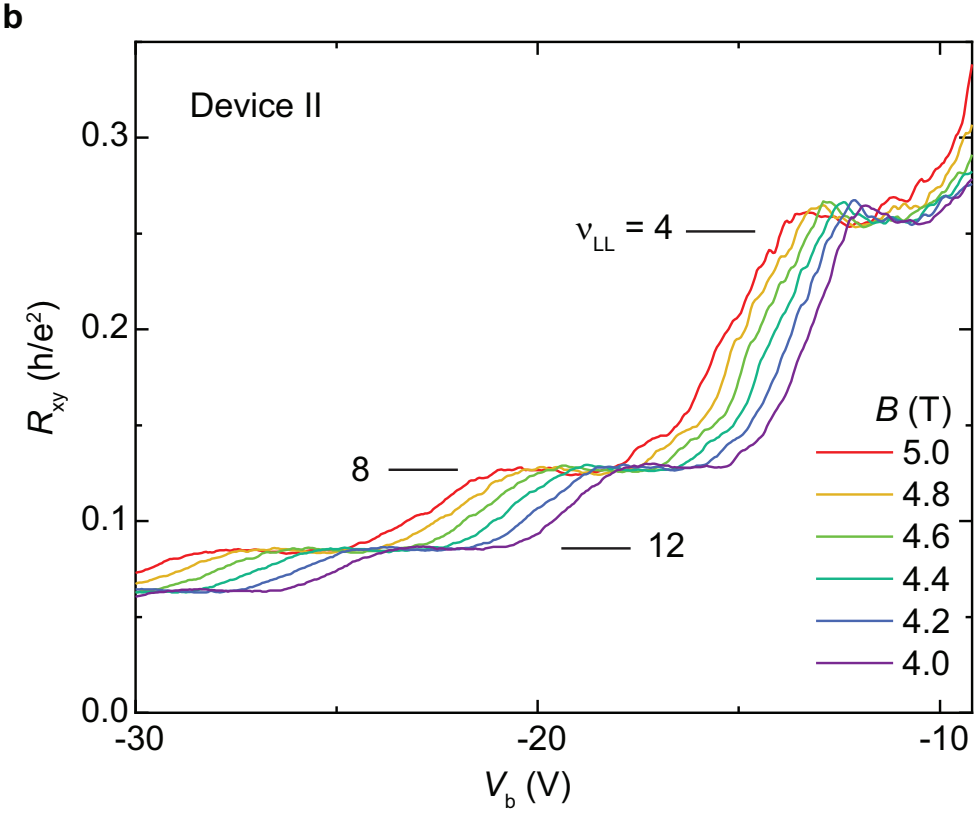
b
Device II
0.3
0.2
0.1
0.0
R_{xy} (h/e^2)
ν_{LL} = 4
8
12
B (T)
5.0
4.8
4.6
4.4
4.2
4.0
-30
-20
-10
V_b (V)

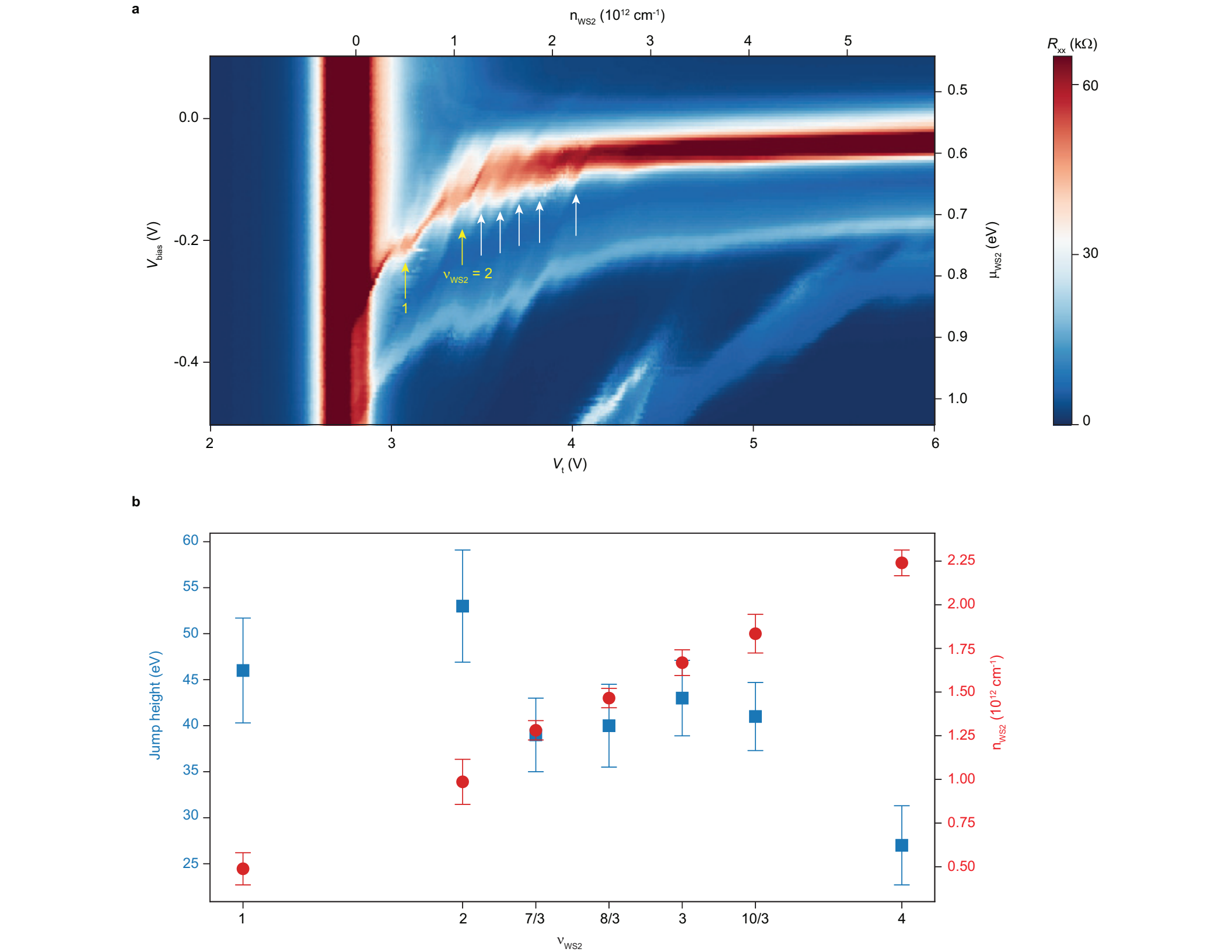
a
n_{WS2} (10^{12} cm^{-1})
0
1
2
3
4
5
R_{xx} (kΩ)
60
30
0
0.0
-0.2
-0.4
V_{bias} (V)
0.5
0.6
0.7
0.8
0.9
1.0
μ_{WS2} (eV)
ν_{WS2} = 2
1
2
3
4
5
6
V_t (V)
b
60
55
50
45
40
35
30
25
Jump height (eV)
2.25
2.00
1.75
1.50
1.25
1.00
0.75
0.50
n_{WS2} (10^{12} cm^{-1})
1
2
7/3
8/3
3
10/3
4
ν_{WS2}

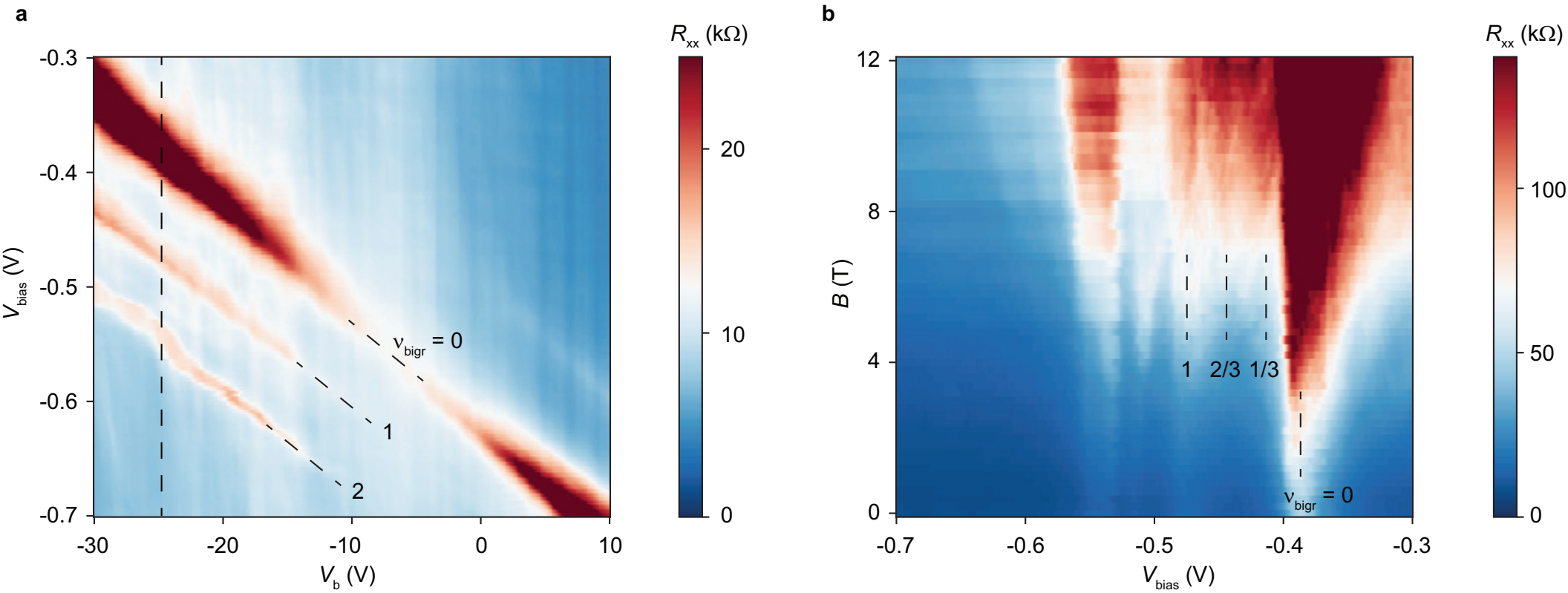
a
b
R_{xx} (kΩ)
V_{bias} (V)
V_b (V)
ν_{bigr} = 0
1
2
B (T)
1 2/3 1/3

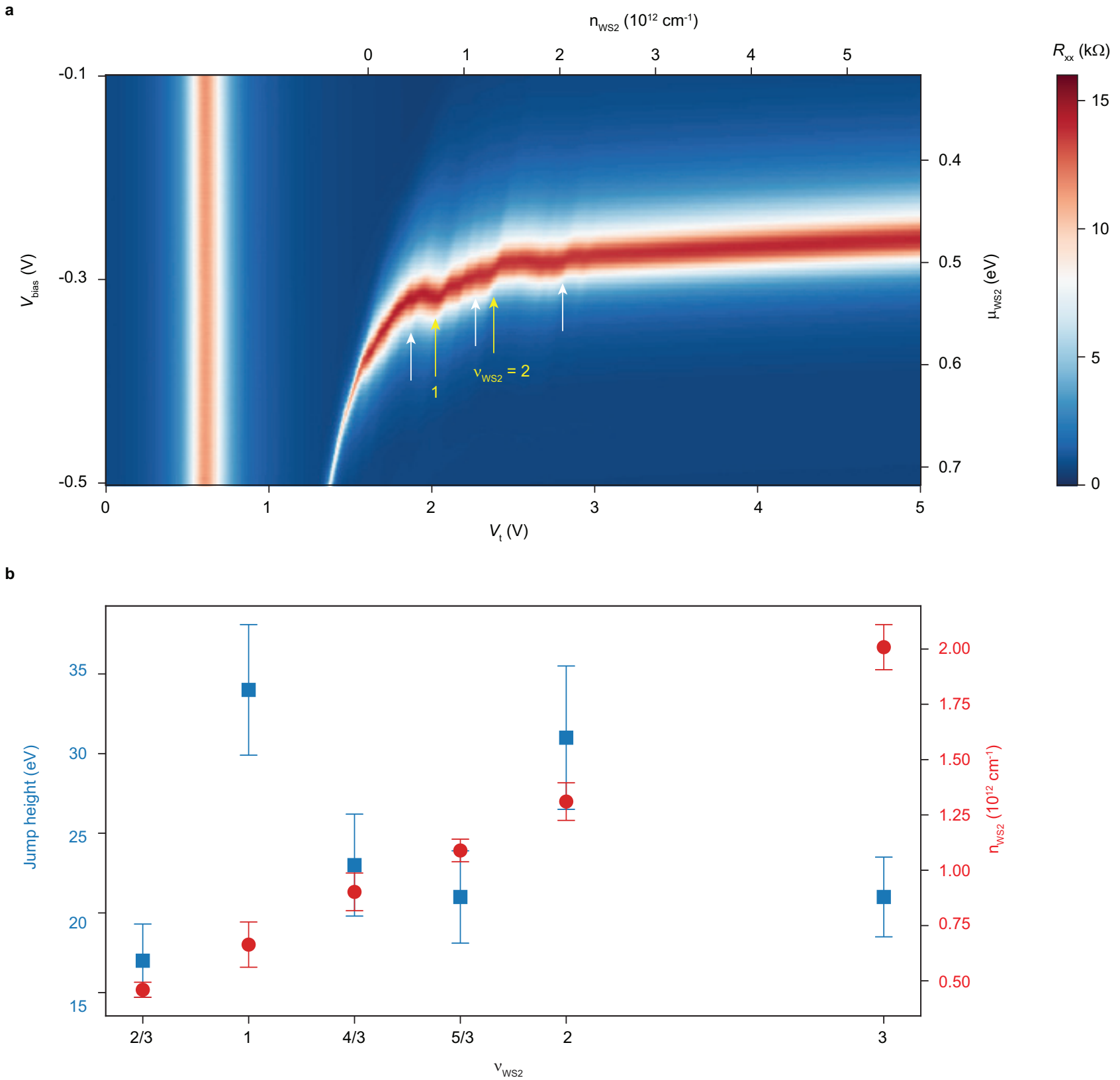
a
n_{WS2} (10^{12} cm^{-1})
0
1
2
3
4
5
R_{xx} (kΩ)
15
10
5
0
-0.1
-0.3
-0.5
V_{bias} (V)
0.4
0.5
0.6
0.7
μ_{WS2} (eV)
ν_{WS2} = 2
1
0
1
2
3
4
5
V_t (V)
b
Jump height (eV)
35
30
25
20
15
n_{WS2} (10^{12} cm^{-1})
2.00
1.75
1.50
1.25
1.00
0.75
0.50
2/3
1
4/3
5/3
2
3
ν_{WS2}